

Semiconductor quantum dots reveal dipolar coupling from exciton to ligand vibration

T. Noblet, L. Dreesen, S. Boujday, C. Methivier, Bertrand Busson, A. Tadjeddine, Christophe Humbert

▶ **To cite this version:**

T. Noblet, L. Dreesen, S. Boujday, C. Methivier, Bertrand Busson, et al.. Semiconductor quantum dots reveal dipolar coupling from exciton to ligand vibration. Communications Chemistry, 2018, 1, pp.76. 10.1038/s42004-018-0079-y . hal-02111047v2

HAL Id: hal-02111047
https://hal.science/hal-02111047v2

Submitted on 20 Nov 2020

HAL is a multi-disciplinary open access archive for the deposit and dissemination of scientific research documents, whether they are published or not. The documents may come from teaching and research institutions in France or abroad, or from public or private research centers.

L'archive ouverte pluridisciplinaire **HAL**, est destinée au dépôt et à la diffusion de documents scientifiques de niveau recherche, publiés ou non, émanant des établissements d'enseignement et de recherche français ou étrangers, des laboratoires publics ou privés.

COMMUNICATIONS CHEMISTRY

ARTICLE

DOI: 10.1038/s42004-018-0079-y OPEN

Semiconductor quantum dots reveal dipolar coupling from exciton to ligand vibration

T. Noblet [1], L. Dreesen[2], S. Boujday [3], C. Méthivier[3], B. Busson [1], A. Tadjeddine[1] & C. Humbert [1]

Within semiconductor quantum dots (QDs), exciton recombination processes are noteworthy for depending on the nature of surface coordination and nanocrystal/ligand bonding. The influence of the molecular surroundings on QDs optoelectronic properties is therefore intensively studied. Here, from the converse point of view, we analyse and model the influence of QDs optoelectronic properties on their ligands. As revealed by sum-frequency generation spectroscopy, the vibrational structure of ligands is critically correlated to QDs electronic structure when these are pumped into their excitonic states. Given the different hypotheses commonly put forward, such a correlation is expected to derive from either a direct overlap between the electronic wavefunctions, a charge transfer, or an energy transfer. Assuming that the polarizability of ligands is subordinate to the local electric field induced by excitons through dipolar interaction, our classical model based on nonlinear optics unambiguously supports the latter hypothesis.

[1] University of Paris-Sud, Université Paris-Saclay, Laboratoire de Chimie Physique, CNRS, Bâtiment 201P2, 91405 Orsay, France. [2] GRASP-Biophotonics, CESAM, University of Liege, Institute of Physics, Allée du 6 août 17, 4000 Liège, Belgium. [3] Sorbonne Université, CNRS, Laboratoire de Réactivité de Surface (LRS), 4 place Jussieu, F-75005 Paris, France. Correspondence and requests for materials should be addressed to C.H. (email: christophe.humbert@u-psud.fr)

Halfway between atomic and solid-state physics, colloidal semiconductor nanocrystals (NCs), also known as quantum dots (QDs), exhibit unique optoelectronic properties arising from their low dimensionality. In such semiconductor nanoparticles, the laser-excited electron-hole pairs are indeed confined in the three spatial directions[1,2]. These excitons are characterized by quantized energies depending on the NC size, and can recombine to emit fluorescence[3,4]. With diameters from 1 to 10 nm, NCs prove optically active over the visible range[5]. As a result, their study falls within the frameworks of many scientific fields: photovoltaics[6], optoelectronics[7], light sources[8], nonlinear optics[9,10], fluorescence spectroscopy[11,] biosensors[12–14] and biomedical imaging[15,16]. For all these reasons, the experimental and theoretical study of QDs is of both applicative and fundamental concerns.

Whether the size-dependent electronic structure of NCs is well understood and described[17–19], a significant number of their fundamental properties is still subject to discussions. For instance, the origin of fluorescence in QDs and the nature of the associated Stokes shift are not well established[20–23], especially since NCs are noteworthy for blinking[24,25]. In essence, the different models developed to account for the processes leading to electron-hole recombination, mainly based on dark excitons[26,27], electron-phonon coupling[28], trap states and charge transfer[29], are not unified. Moreover, when NCs are functionalized, their coupling to the molecular ligands is expected to play a key role. Potential vibroelectronic interactions between NCs and molecules must be taken into account and make the description of QDs more complex. In this context, most of the studies focus on the influence of ligands on the optoelectronic properties of NCs[30–37]. In particular, some-specific surface modifications with organic ligands proved to enhance light absorption and fluorescence emission[38–40], which is a clear advantage for photovoltaic, photodetection and photoemission applications. It has also been shown that ligands condition the quantum confinement and the phonon behaviour of NCs, thus affecting exciton dynamics and transport phenomena[41–43]. It is worth noting that the exciton-phonon coupling and the interplay between electronic and mechanical properties of NCs has been deeply studied, leading especially to evidence the influence of ligands on the lattice vibrations of NCs[43]. In order to supplement these analyses of QD/ligand interactions, here we characterize and explain the influence of QD excitons on the vibrational properties of the ligands. We then directly probe the ligands and examine their vibration modes to investigate in this manner how the electronic properties of NCs are coupled to the mechanical behaviour of their ligands. This work is all the more relevant that the study of surface properties is one of the most fundamental aspect of QDs. Contrary to the excitonic behaviour of the core, which is realistically well understood, the coupling of the QD states to their direct chemical environment, and then to the ligand states, is still under discussion[44]. Within this framework, this article demonstrates experimentally and theoretically the correlation between the electronic structure of NCs and the vibrational structure of ligands, and also brings significant information about the surface and ligand chemistry of commonly used QDs, addressing thereby fundamental and practical issues.

Here, the experimental evidence is adduced through two-colour sum-frequency generation (2C-SFG) spectroscopy combining visible and infrared laser beams on commercial ligand-conjugated CdTe NCs, as it is properly dedicated to characterizing vibroelectronic interactions at interfaces and probing the surface chemistry[10,45–47]. As a second-order optical process, SFG is indeed doubly resonant, with respect to both the visible and the infrared, and surface specific. For instance, SFG spectroscopy has already proved relevant for the study of electron-phonon coupling within fullerene thin films[48]. In our case, 2C-SFG is performed in total internal reflection configuration with a deposition of CdTe NCs on CaF_2 prism (Fig. 1a) to benefit from favourable Fresnel factors[49]. Our results evidence five ligand vibration modes whose amplitudes depend on the visible frequency, ω_{vis}, and are maximum when ω_{vis} coincides with the energy of the first excitonic state of NCs. Besides this, from a chemical point of view, 2C-SFG reveals the presence of unexpected residual hydrophobic ligands at the surface of these commercial NCs, suggesting the incompleteness of ligand exchange during their synthesis and functionalization.

We also demonstrate that a classical dipolar interaction between NCs and molecules is sufficient to describe their coupling as unveiled by nonlinear optics, which is evidence in support of an energy transfer-based process. Within this theoretical model, the predicted ω_{vis}-dependence of the ligand vibration amplitudes fits very well the measurements obtained with 2C-SFG spectroscopy. Consequently, this work enhances the understanding of the coupling between QDs and ligands and ensures that the vibrational properties of the molecular surroundings is well correlated to NCs' excitons.

Results

From linear to nonlinear optical response of QDs. The comprehension of the coupling between CdTe NCs and their ligands requires first and foremost the characterization of their optoelectronic properties. In our case, we preliminary need to model the linear dielectric susceptibility $\chi^{(1)}_{QD}$ of NCs as it governs their electronic response to a visible excitation and enables the structural characterization of the QD layer once deposited on CaF_2 prism. In order to model $\chi^{(1)}_{QD}$, we measure the UV-visible absorbance $\mathcal{A}(\omega)$ spectrum of a reference colloidal solution as featured in Fig. 2a. The fit is obtained thanks to the quantum analytical expansion of $\chi^{(1)}_{QD}$ stated in Supplementary Methods (Supplementary Tables 1–3). This reveals quite large dipole moments, around 15 D. Given previous works, such oscillator strengths are expected for semiconductor nanocrystals[50,51]. Excitons thus can be seen as highly polar electron-hole pairs, which confirms that CdTe QDs exhibit an important dielectric response and constitute good optical probes. The knowledge of $\chi^{(1)}_{QD}$ enables thereupon to finely characterize the deposition of CdTe NCs on the substrate. Especially, the QD density and the refractive index of the layer are essential for computing the Fresnel factors which drive the layer reflectivity in nonlinear optics.

Figure 2b shows the absorbance spectrum of the QD layer. As explained in Supplementary Methods, its fit leads to a surface density of $6.6 \times 10^{18}\ m^{-2}$ and a size dispersion of 5%. The layer thickness is henceforth estimated to 255 nm. This dense layer is expected to affect the Fresnel factors of the CaF_2/QD/air interface through its refractive index $n_{lay}(\omega) = \sqrt{1 + \chi^{(1)}_{QD}(\omega)}$[52]. Figure 2c shows the four SFG Fresnel coefficients L_{ijk} which contribute to the SFG signal in our configuration as computed with the three-layer model (see Supplementary Methods and Supplementary Fig. 1). In this $\mathcal{PPP}$-polarization scheme, the SFG intensity I_{SFG} of the sample is proportional to the input intensities I_{vis} and I_{IR}: $I_{SFG} \propto |\chi^{(2)}_{\mathcal{PPP}}|^2 I_{vis} I_{IR}$[53]. The effective second-order susceptibility $\chi^{(2)}_{\mathcal{PPP}}(\omega_{vis}, \omega_{IR})$ of the probed interface encodes physically and mathematically its vibroelectronic response and is actually the quantity that we extract from SFG spectroscopy. Given the geometry of the sample, $\chi^{(2)}_{\mathcal{PPP}}$ is only related to four components

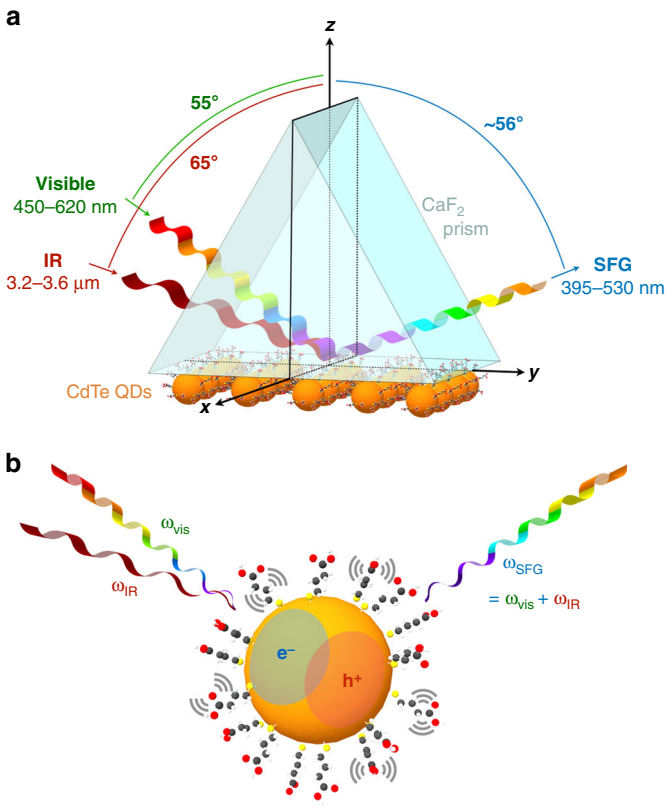


Fig. 1 Experimental configuration. **a** Ligand-conjugated CdTe QDs are deposited on a CaF_2 prism and probed by 2C-SFG spectroscopy. The visible, IR and SFG beams belong to the incidence plane (y, z), like their respective polarizations as they are all $\mathcal{P}$-polarized. This configuration is known as $\mathcal{PPP}$-polarization scheme. **b** The visible beam, at frequency ω_{vis}, excites NCs by creating confined electron-hole pairs (e^-, h^+) called excitons, while the IR beam, at frequency ω_{IR}, excites vibration modes of their ligands. The SFG beam is generated as a combination of both, and as a signature of the NC/ligand vibroelectronic coupling

of the second-order susceptibility tensor $\boldsymbol{\chi}^{(2)} = (\chi^{(2)}_{ijk})$[53]:

$$\begin{aligned}\chi^{(2)}_{\mathcal{PPP}} = &-L_{xxz}\cos\theta_{\mathrm{SFG}}\cos\theta_{\mathrm{vis}}\sin\theta_{\mathrm{IR}}\,\chi^{(2)}_{xxz}\\ &-L_{xzx}\cos\theta_{\mathrm{SFG}}\sin\theta_{\mathrm{vis}}\cos\theta_{\mathrm{IR}}\,\chi^{(2)}_{xzx}\\ &+L_{zxx}\sin\theta_{\mathrm{SFG}}\cos\theta_{\mathrm{vis}}\cos\theta_{\mathrm{IR}}\,\chi^{(2)}_{zxx}\\ &+L_{zzz}\sin\theta_{\mathrm{SFG}}\sin\theta_{\mathrm{vis}}\sin\theta_{\mathrm{IR}}\,\chi^{(2)}_{zzz}.\end{aligned} \quad (1)$$

The angles $\theta_{\mathrm{vis}} = 55°$, $\theta_{\mathrm{IR}} = 65°$ and $\theta_{\mathrm{SFG}} \sim 56°$ are sketched in Fig. 1. As said before, the Fresnel factors L_{ijk} modulate the nonlinear response. Thanks to Fig. 2c, it is worth noting that the zzz Fresnel factor prevails over the others which are, in addition, fairly flat over the range 450–620 nm. Indeed, the presence of QDs shows through in the zzz term of Eq. (1), related to the z-components of the electric fields which probe most effectively the QD layer. The effective second-order susceptibility $\chi^{(2)}_{\mathcal{PPP}}$ is consequently restricted to the zzz term on which we focus:

$$|\chi^{(2)}_{\mathcal{PPP}}| \sim |L_{zzz}(\omega_{\mathrm{vis}},\omega_{\mathrm{IR}})\,\chi^{(2)}_{zzz}(\omega_{\mathrm{vis}},\omega_{\mathrm{IR}})|. \quad (2)$$

Figure 2c also evidences that $|L_{zzz}|$ is a monotonic function of the visible wavelength λ_{vis} on the range 450–620 nm. If the effect of QDs on the SFG response only depended on the Fresnel factors, we would expect $|\chi^{(2)}_{\mathcal{PPP}}|$ to be enhanced for $\lambda_{\mathrm{vis}} = 450$ nm by a factor of 1.2 with respect to 612 nm (Fig. 2c). As shown in the following, such a Fresnel effect cannot account for the shape nor the amplitude of the SFG response over the visible range. The coupling between NCs and ligands is consequently linked to $\chi^{(2)}_{zzz}$ and genuinely related to the fundamental properties of QDs.

Chemical characterization of commercial QDs. The QDs we use in this work are commercial CdTe NCs bearing terminal carboxylic acid groups (COOH). The synthesis and surface composition of these crystals are poorly described by the supplier, and parameters such as the chain length are unknown. Hence, before investigating the NC/ligand coupling with 2C-SFG spectroscopy, we performed a deep characterization of the starting material. In Fig. 3, energy dispersive X-ray measurements (EDX) and X-ray photoelectron spectroscopy (XPS) reveal the presence of multiple elements in addition to Cd and Te: mainly carbon and oxygen, but also an important amount of sulfur. We thus deduce that NCs surface functionalization is achieved using mercaptocarboxylic acids (MCAs) with the molecular formula HS-$(CH_2)_n$-COOH, as described in the literature for CdTe NCs coating[54,55]. Their maximum chain length is estimated from the ratio carbon to sulfur that leads to $n \leq 4$: the carbon atoms engaged in the COOH functional groups, featured in Fig. 3c, indeed represent 20% of the total carbon. Going deeper into S_{2p} photopeak analysis (Fig. 3d), we can see two doublets at different binding energies showing that there are two different populations of sulfur. To understand the origin of these populations, we compare S_{2p} photopeaks of QDs before and after ion sputtering. This treatment allows the removal of the ligands from NCs surface, as evidenced by the decrease of the C_{1s} photopeak. The removal of the ligands after ion sputtering is confirmed by the oxidation of Cd and Te on the no-longer passivated NCs upon exposure to the air (Fig. 3d). Interestingly, on S_{2p} photopeak, the ion sputtering leads to a considerable decrease of the higher-energy S_{2p} doublet (in light grey) whereas the lower-energy one (in deep grey) remains unchanged. We therefore conclude that the first population of sulfur was removed with MCA ligands while the second one is located within the NCs core. This observation explains the ratio Cd/Te superior to 1 shown by the EDX spectrum (Fig. 3a) and the XPS measurements (Fig. 3d). Obviously, metal chalcogenides are well-known for showing metal-rich stoichiometries, mainly due to an excess of metal ions in the surface layer[56,57]. Yet, this excess is reported to lead to a metal/chalogenide ratio from 1.1 to 1.2, depending on the nanoparticle geometry[57,58]. Our findings evidence a Cd/Te ratio around 4, which is far too high to be related to a surface excess of cadmium. As a consequence, the commercial QDs are not purely CdTe NCs as claimed by the manufacturer, but consist in ternary alloys $CdTe_xS_{1-x}$ with $x = 0.25$. As the sulfur and tellurium are both chalcogen atoms, the substitution of Te by S does not critically change the crystal structure. This structure has indeed been characterized by high resolution transmission electron microscopy in ref. [59]. In addition, as discussed in Supplementary Note 1, the value $x = 0.25$ is compatible with our UV-visible measurements. It is then worth noting that it does not impact our study since the optoelectronic properties of QDs are completely characterized by UV-visible spectroscopy: the mere knowledge of their dielectric susceptibility $\chi^{(1)}_{\mathrm{QD}}$ is sufficient to account for the role they play in 2C-SFG spectroscopy.

Surface chemistry of QDs revealed by 2C-SFG. Phenomenologically, for a given visible frequency, the effective second-order susceptibility is modelled over the IR spectral range

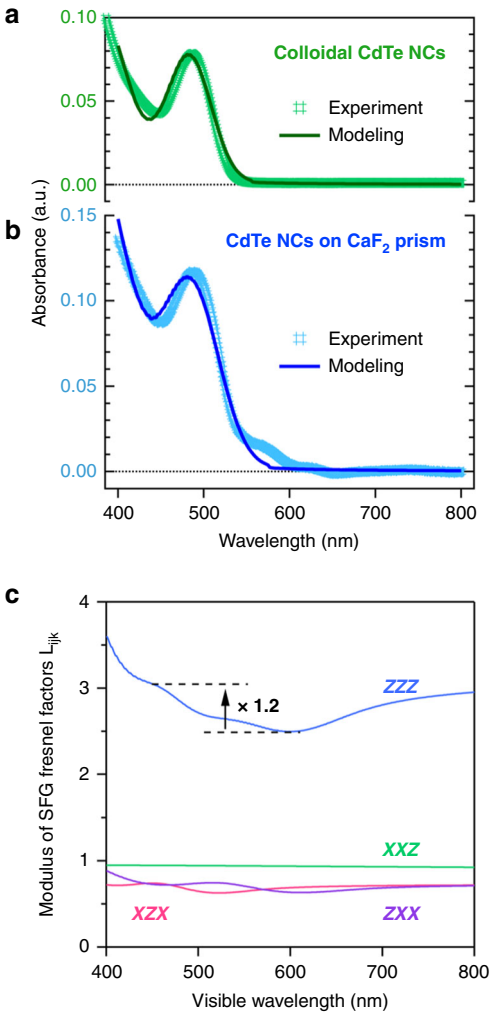


Fig. 2 Optical response of QDs over the visible range. UV-visible absorbance spectra of **a** the colloidal CdTe NCs solution (concentration of 3.66×10^{20} m^{-3}) and, **b** the CaF_2 prism grafted with CdTe NCs. The solid lines corresponds to their respective modellings (Supplementary Methods). **c** Modulus of SFG Fresnel factors L_{ijk} with respect to the visible wavelength. The IR frequency is set at 2900 cm^{-1}. In $\mathcal{PPP}$ configuration, the only four contributions are given for $ijk = xxz, xzx, zxx, zzz$ (Eq. (1)). The computation, performed within the 3-layer modelling of CaF_2/QD/air interface, is detailed in Supplementary Methods (Supplementary Fig. 1)

according to[10]:

$$\chi^{(2)}_{\mathcal{PPP}} = A\, e^{i\Phi} + \sum_{v} \frac{a_v}{\omega_v - \omega_{\mathrm{IR}} + i\gamma_v}. \qquad (3)$$

The first term depicts the non-resonant response (in the IR range) of the inorganic components of the interface (i.e. CaF_2 and NCs), whereas the second term, which consists in a sum over vibration modes v, accounts for the resonant response of the molecules localized at the surface (i.e. ligands). On this assumption, each vibration mode v of the organic ligands is modelled by a lorentzian function, which is maximum when the IR frequency ω_{IR} coincides with the eigenfrequency ω_v of the mode; a_v is therefore its amplitude and γ_v the associated damping constant. The phase shift Φ included in the non-resonant contribution represents a would-be phase delay between the SFG responses of the inorganic components and the molecules. SFG spectra are normalized to extract $|\chi^{(2)}_{\mathcal{PPP}}|^2$ (Supplementary Methods), then Eq. (3) is used to fit them and to locate the vibration modes. As evidenced in the previous section, the commercial QDs we use are conjugated with MCAs, so that we expect to identify the methylene groups (CH_2) of their aliphatic chains in the IR range 2750–3050 cm^{-1}.

We acquired five SFG spectra of the CaF_2/QD sample with five different visible wavelengths: 450, 488, 520, 568 and 612 nm. The data, presented in Fig. 4, are fitted thanks to Eq. (3) by taking five vibration modes into account (Supplementary Table 4). We identify the symmetric (CH_2,ss at 2862 cm^{-1}) and asymmetric (CH_2,as at 2935 cm^{-1}) stretching modes of methylene groups. A third mode associated to CH_2 is also located at 2912 cm^{-1}. According to different studies about MCAs, this exotic stretching mode (CH_2,xs) can be both assigned to the d^-_ω asymmetric mode of CH_2[60] or described as coming from the symmetric stretching of a methylene group linked to a heteroatom (sulfur in our case) [47]. As a matter of fact, this mode may arise from a combination of the two, hence a much higher vibration amplitude (Fig. 4a, b), around twice greater than the others. Either way, these three modes have already been observed for 11-mercaptoundecanoic acid with SFG spectroscopy[60], which is in agreement with the presence of MCAs. Moreover, the SFG spectra evidence the presence of methyl groups. We indeed identify their symmetric (CH_3,ss at 2884 cm^{-1}) and asymmetric (CH_3,as at 2967 cm^{-1}) stretching modes[47,60], although their amplitudes are weaker than those of methylene. These methyl groups cannot originate from MCA ligands. But, we know that the synthesis and stabilization of CdTe NCs are commonly achieved in organic solvents thanks to hydrophobic ligands like trioctylphosphine oxide, dodecanethiol or tetraoctylammonium bromide, before these are substituted by hydrophilic MCAs for the transfer of NCs into aqueous phase[4,12,55,61]. All these hydrophobic ligands exhibit CH_3 groups. Thereby, our measurements show the incompleteness of the ligand substitution throughout the chemical preparation of QDs made by the manufacturer. Here, SFG spectroscopy reveals methyl residues probably originating from QD synthesis and stabilization processes. Looking back at XPS measurements, these residues are expected to contribute to the total carbon detected on QDs (Fig. 3c). This means that the structure of MCAs is of the type HS-$(CH_2)_n$-COOH with $n < 4$ (and not $n \leq 4$). Given the literature[4,54,55], MCAs are probably 3-mercaptopropionic acids ($n = 2$). It would imply that the hydrophobic ligands account for 20–40% of the total carbon (in terms of number of carbon atoms, not of ligands). As a result, this observation confirms that ligand exchange is a critical process with a limited efficiency and that the mechanisms involved are still not properly understood[62]. In all likelihood, CdTe NCs are here coated with a majority of MCAs and a few residual hydrophobic ligands.

Vibroelectronic correlation in ligand-capped QDs. Given the five vibration modes previously identified, we examine the evolution of their amplitudes with respect to the visible wavelength λ_{vis}. Especially, Fig. 4b turns into picture the results extracted from the SFG spectra for the five vibration modes. We clearly see that the vibration amplitudes are maximum in the case where $\lambda_{\mathrm{vis}} = 488$ nm. Indeed, the SFG spectrum obtained for this visible wavelength is the most intense and resolved in Fig. 4a. As shown in the UV-visible spectrum reminded in Fig. 4b, $\lambda_{\mathrm{vis}} = 488$ nm corresponds to the local maximum of absorption of CdTe NCs, *id est* their first excitonic state. Besides, the evolution of each vibration amplitude as a function of λ_{vis} is not monotonic over the studied range. As argued before, this behaviour cannot be related to Fresnel factors, and thus evidences a fundamental coupling between the electronic properties of QDs, whose optical activity is maximum when $\lambda_{\mathrm{vis}} = 488$ nm, and the vibrational

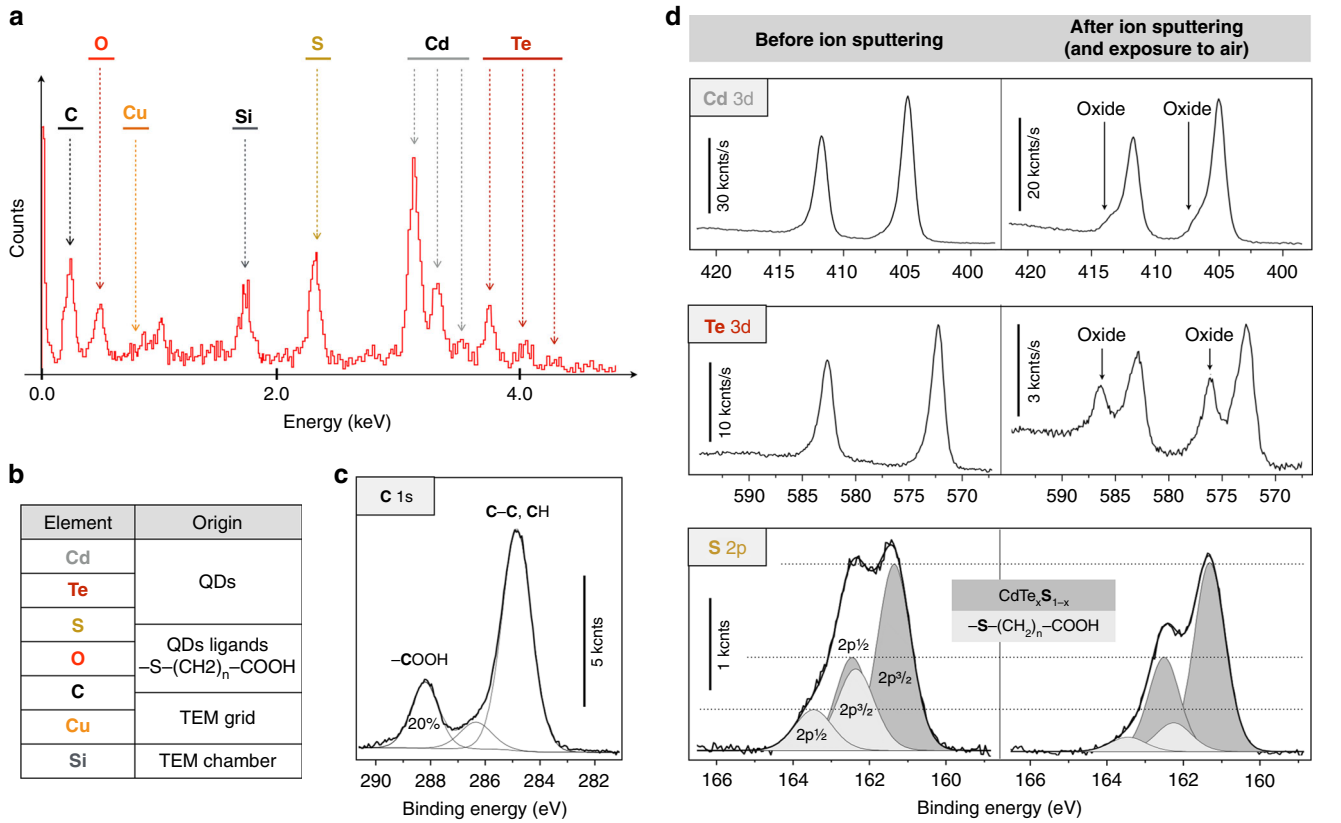


Fig. 3 Chemical characterization of the commercial COOH-conjugated CdTe quantum dots. **a** EDX spectrum of CdTe NCs deposited on a carbon-coated copper grid. **b** Table gathering all the chemical elements detected by EDX spectroscopy and indicating their origins. **c** XPS spectrum of CdTe NCs deposited on a silicon wafer related to carbon (1s state). **d** XPS spectra of CdTe NCs deposited on a silicon wafer related to cadmium (3d states), tellurium (3d states) and sulfur (2p states). In order to compare NCs with and without their ligands, XPS measurements are performed before (spectra on the left-hand side) and after (spectra on the right-hand side) ion sputtering of the sample (and exposure to air in the case of Cd and Te)

response of their ligands, which is here concomitantly optimal when $\lambda_{vis} = 488$ nm. Further, to quantify the efficiency of this coupling for each vibration mode ν, we define the factor F_ν as the ratio between its amplitudes measured for 488 and 612 nm:

$$F_\nu = \frac{a_\nu(\lambda_{vis} = 488\,\mathrm{nm})}{a_\nu(\lambda_{vis} = 612\,\mathrm{nm})}. \quad (4)$$

The amplitude a_ν at 612 nm is chosen as a reference because the absorbance of NCs at this wavelength is very close to zero, which means that they are much less optically active at this wavelength. Nevertheless, regarding Fig. 4b, the vibration amplitudes are clearly not proportional to the QD absorbance: assuming such a proportionality would lead to a factor F_ν up to 42.5, largely exceeding the values indicated in Fig. 4b. We conclude that the absorbance itself is not enough to describe and account for the QD/ligand correlation. In addition, for all the vibration modes, F_ν is greater than the factor 1.2 defined in Fig. 2c: $\bar{F}_\nu$ is up to 2.5 on average, and definitively excludes any effect of Fresnel factors. The question is how to theoretically account for this factor, and thus for the QD/ligand coupling.

Discussion

CdTe NCs have just been proved to maximize the vibrational response of their ligands when they are optically pumped into their first excitonic state. Such an exciton can be seen as a highly polar electron-hole pair of dipole moment $\mathbf{p}$ generated by the incident electric field $\mathbf{E}$. From this dielectric point of view, the ligands feel the local electric field $\mathbf{E}_\ell(\omega) \propto \mathbf{p}(\omega) \propto \boldsymbol{\chi}^{(1)}_{QD}(\omega)\mathbf{E}(\omega)$ produced by the exciton. This excitonic field is expected to change the molecular dipole moment $\boldsymbol{\mu}$ of the ligands and to enlarge their SFG cross-section. Indeed, we can write $\mu(\omega) = \boldsymbol{\alpha}(\omega)\mathbf{E}_\ell(\omega) + \mu_\mathbf{0}$, where $\boldsymbol{\alpha}$ is the polarizability of molecules and $\boldsymbol{\mu}_0$ their dipole moment in the absence of exciton. After they absorb IR light, ligands acquire an oscillating dipole moment with a certain amplitude $\Delta\boldsymbol{\mu}$, then related to $\boldsymbol{\alpha}$ and $\boldsymbol{\chi}^{(1)}_{QD}$: the NC/ligand coupling is embodied by the product of these two dielectric functions, hence its dipolar nature. The calculations of $\Delta\boldsymbol{\mu}$ are derived in details in Supplementary Notes 2–4 and show that the SFG intensity, related to $\langle\Delta\boldsymbol{\mu}(t)^2\rangle$, involves a second-order susceptibility whose form is:

$$\chi^{(2)}_{ijk}(\omega_{vis}, \omega_{IR}) = g_k \frac{\left[\partial\boldsymbol{\alpha}(\omega_{vis}) \cdot \boldsymbol{\chi}^{(1)}_{QD}(\omega_{vis})\right]_{ij}}{\omega_\nu - \omega_{IR} + i\gamma_\nu}, \quad (5)$$

for each vibration mode ν with the eigenenergy ω_ν and the damping constant γ_ν. g_k is a constant related to the geometry of molecules. The quantity $\partial\boldsymbol{\alpha}$ corresponds to the spatial derivative of $\boldsymbol{\alpha}$ with respect to the normal coordinate of mode ν. $\partial\boldsymbol{\alpha}(\omega_{vis})$ can be considered as the Raman-like cross-section of the ligands under a visible excitation[63]. Thus, the numerator in Eq. (5), which completely conditions the amplitude of the vibration mode ν, explicitly embodies the coupling between NCs (through $\boldsymbol{\chi}^{(1)}_{QD}$) and molecules (through $\partial\boldsymbol{\alpha}$) occurring with a visible excitation light. Hence, the vibration amplitude is expected to be maximum when ω_{vis} is in resonance with excitonic states (because of $\boldsymbol{\chi}^{(1)}_{QD}$) and when the Raman activity of the vibration mode ν is significant

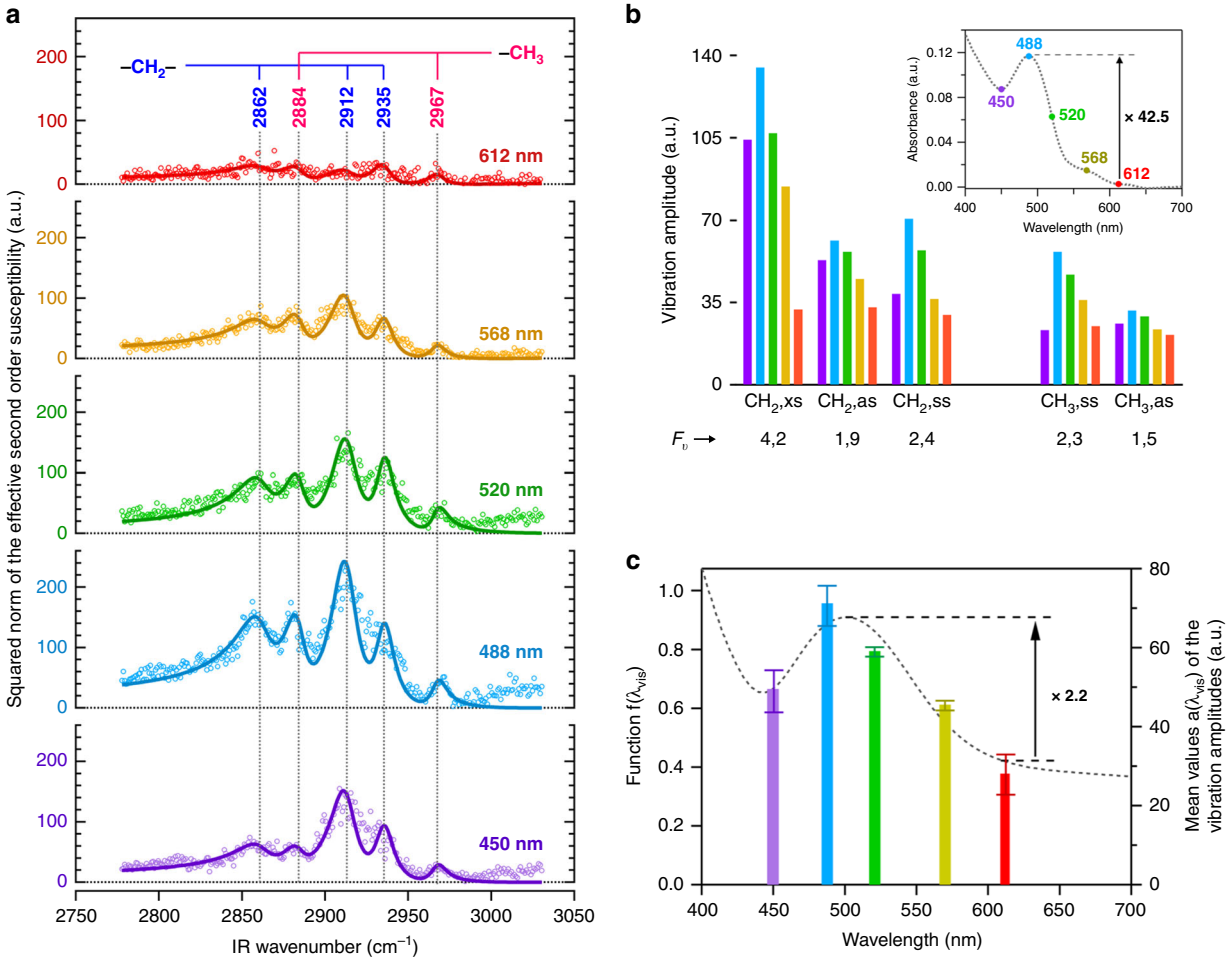


Fig. 4 Evidence and modelling of the vibroelectronic correlation between NCs and ligands. **a** 2C-SFG spectra of CaF_2/QD/air interface. These spectra consist in performing the vibrational spectroscopy of the sample over the IR range 2750–3050 cm^{-1} for five different fixed visible wavelengths λ_{vis}. The corresponding values of λ_{vis} are indicated in nanometres on the right. The bold curves are fits to the experimental data. The vertical dotted lines locate the five C–H stretching vibration modes used for this fitting (Supplementary Table 4), coming from methylene and methyl groups. **b** Vibration amplitudes a_v associated to the five C–H stretching modes according to the visible wavelength. The values are extracted from the fitting of the SFG spectra (Supplementary Table 4). The UV-visible absorbance spectrum of the CaF_2/QD sample (Fig. 2b) is inserted at the top right hand corner to locate the five visible wavelengths. Below each vibration mode, we give the factor F_v calculated according to Eq. (4). **c** Superposition of, i, the function $f(\lambda_{vis})$ (grey dotted curve) defined in Eq. (7) and calculated with $\omega_v = 2900$ cm^{-1} and, ii, the mean vibration amplitudes (colour bars) computed over the five vibration modes for each visible wavelength. The calculation of the error bars is explained in Supplementary Methods and with Supplementary Fig. 2

(because of $\partial\boldsymbol{\alpha}$). In $\mathcal{PPP}$ configuration, Eq. (2) now reads:

$$|\chi^{(2)}_{\mathcal{PPP}}| \sim \frac{|L_{zzz}(\omega_{vis},\omega_{IR})\, g_z\, \partial\alpha_{zz}(\omega_{vis})\, \chi^{(1)}_{QD}(\omega_{vis})|}{|\omega_v - \omega_{IR} + i\gamma_v|}. \quad (6)$$

A priori, $\partial\alpha_{zz}$ does not resonate with the visible beam because the ligands do not exhibit electronic transition in the probed visible range. For each mode v, the ω_{vis}-dependence of its vibration amplitude is then mainly driven by the function:

$$f(\omega_{vis}) = |L_{zzz}(\omega_{vis},\omega_v)\, \chi^{(1)}_{QD}(\omega_{vis})|. \quad (7)$$

In virtue of our previous calculations of Fresnel factors and $\chi^{(1)}_{QD}$, we draw this function in Fig. 4c with respect to λ_{vis}. Unlike the absorbance, related to the imaginary part of $\chi^{(1)}_{QD}$, $f(\lambda_{vis})$ does not cancel at 612 nm. This comes from the real part of $\chi^{(1)}_{QD}$ which characterizes the optical dispersion of QDs. In order to appreciate the accuracy of Eqs. (5) and (6), we compare the function $f(\lambda_{vis})$ with the mean vibration amplitudes $\bar{a}(\lambda_{vis}) = \frac{1}{5}\sum_v a_v(\lambda_{vis})$ computed over the five vibration modes v for the five visible wavelengths. In Fig. 4c, to achieve this comparison, we align the origins of the two scales and distend the axis of $\bar{a}(\lambda_{vis})$ so that the errors bars overlap with the curve of $f(\lambda_{vis})$. As we can see, the function $f(\lambda_{vis})$ satisfactorily accounts for the λ_{vis}-dependence of the vibration amplitudes. In particular, it provides for a factor $\bar{F}_v$ up to 2.2, close to experimental value of 2.5. The shape of $f(\lambda_{vis})$ predicted by our model is therefore compatible with our measurements and effectively accounts for the coupling between NCs and ligands.

Ascribing this vibroelectronic correlation to a dipolar interaction between NCs and ligands may appear in contradiction with the extensive literature available on this issue. As mentioned in the introduction, surface trapping, charge transfer, exciton delocalization and orbital mixing are generally invoked to explain the electronic coupling between the core and the ligands[39,64]. But all these experimental works investigate the NC/ligand coupling through the monitoring of the optoelectronic behaviour of QDs, whereas we here examine this coupling by scrutinizing the vibrational behaviour of the ligands. As linear alkane chain

molecules, these ligands ensure that QDs are mainly trap-free and do not experience charge transfer, given the insulating nature of the ligand chains, unlike π-conjugated ligands[39,65]. This point is even corroborated by our previous photoluminescence measurements, which showed that these QDs do not suffer from fluorescence quenching, despite their conjugation with short ligands[59]. Henceforth, we do not expect the coupling observed with 2C-SFG spectroscopy to be based on the same mechanisms than those which describe ligand-dependent optoelectronic properties of the core. It is also worth noting that our study deals with a QD thin film. In such a solid phase, ligands have already proved to play a leading role on the effective polarization of the QD surroundings and their excitonic properties[66]. The existence of such dielectric effects from ligands to excitons actually allows us to conceive other mechanisms than surface trapping and charge transfer, and to base our reasoning on the assumption of a dipolar coupling from excitons to ligand vibrations. The association of these two studies thus emphasizes the importance of dipolar/dielectric coupling between NCs and ligands: in both cases, the interplay between QDs and capping molecules is driven by their respective dielectric functions.

To conclude, the originality of this work relies on the direct investigation of NC/ligand vibroeletronic coupling with 2C-SFG spectroscopy that evidences without ambiguity a correlation between the electronic and the vibrational structures of functionalized QDs. As predicted with simulations in Raman spectroscopy[67] but not observed before now, pumping QDs in their excitonic states translates into fostering the vibrational response of their surrounding organic environment. Comparing the vibrational amplitudes of methyl and methylene modes of the ligands at the visible wavelengths 488 nm (first excitonic state) and 612 nm (out of excitonic resonance), we measured on average a gain factor of $\bar{F}_v^2 = 6.3$ in terms of SFG intensity. This experimental demonstration is all the more relevant that SFG spectroscopy has been performed on a ~0.3 µm-thickness QD layer made of 3.4 nm-diameter particles, which is very small with regard to the interfaces more commonly studied (~5 µm-thickness layers of 30–100 nm particles[68]). Thus, we succeeded in characterizing the NC/ligand coupling in a case which is not particularly favourable. Furthermore, the theoretical modelling that we developed to describe this coupling concludes here in favour of an energy transfer-based process, rather than a charge transfer[67,69]. Our formal calculations showed that a classical dipolar interaction can account for the results, considering that the polarizability of the molecules is subordinate to the local electric field induced by the excitons. Besides, the generality and the simplicity of this approach, only based on dielectrics, make it useful and applicable to other systems within the framework of nonlinear optics.

Methods

CdTe QD preparation. CdTe QDs were purchased from Sigma-Aldrich: Ref. 777935 CdTe core-type 25 mg (www.sigmaaldrich.com/catalogue/product/aldrich/777935). These commercial CdTe QDs are coated with carboxylic acid functional ligands (COOH) and are provided through water-soluble powders. According to ref. [59], their mean radius is $R_0 = 1.7 \pm 0.3$ nm. The stock solution was prepared in Milli-Q water (18 MΩ cm, Millipore, France) for a QD density $N = 3.66 \times 10^{20}$ m^{-3} (i.e. ~0.6 µM). To deposit QDs on substrate, an equilateral CaF_2 prism (Fichou, flatness: $\lambda/4$ at 633 nm) was first washed in acetone (99.8%, Sigma-Aldrich) and ethanol (99.8%, Sigma-Aldrich) using a sonication bath, and then cleaned with a piranha solution (H_2O_2 30%:H_2SO_4 96%, 1:2, Sigma-Aldrich). It is rinsed with Milli-Q water (18 MΩ cm, Millipore, France) and dried under nitrogen gas flow. The deposition of CdTe QDs consisted in spreading a droplet of the stock solution on one face of the prism and drying it with nitrogen.

UV-visible spectroscopy. UV-visible absorbance spectra of the colloidal solution and the CaF_2/QD sample were both recorded using a Cary-5000 spectrophotometer (Agilent) in transmission. Milli-Q water was used as a reference for the solution (in a PMMA cuvette of pathlength $\ell = 1$ cm) and a bare CaF_2 prism for the CaF_2/QD sample. The absorbance curves are thus obtained by differential measurements.

Energy dispersive X-ray spectroscopy. Chemical analyses were performed with a JOEL JEM 2010 transmission electron microscope operating at 200 kV fitted with an energy dispersive X-ray (EDX) spectrometer PGT-Imix-PC. QDs were deposited on carbon-coated copper grids.

X-ray photoelectron spectroscopy. XPS spectra were collected on a SPECS GmbH PHOIBOS 100-1D delay line detector photoelectron spectrometer, using a monochromated AlKα ($h\nu = 1486.6$ eV) radiation source having a 250 W electron beam power. The sample was analyzed under ultra-high vacuum conditions (1×10^{-8} Pa). After recording a broad range spectrum (pass energy 100 eV), high resolution spectra were recorded for the C_{1s}, S_{2p}, Te_{3d}, Cd_{3d} core XPS levels (pass energy 20 eV). The peak areas were determined after subtraction of a Shirley background. The atomic ratio calculations were performed after normalization using Scofield factors. Spectrum processing was carried out using the Casa XPS software package. The sputtering of the QDs were performed in the XPS chamber using a 2 keV Ar^+ beam.

Nonlinear SFG spectroscopy. Vibrational SFG spectra were acquired thanks to a home-made setup described in ref. [70]. A pulsed IR laser source (Nd:YVO_4, 1064 nm, 7.5 ps, HighQ laser) is coupled to an acousto-optic modulator (62.5 MHz micropulse repetition rate, 2 µs train, 25 Hz macropulse repetition rate) and is used, after amplification, to pump two optical parametric oscillators (OPO): i, an IR OPO tunable in the 2500–4000 cm^{-1} spectral range and, ii, a visible OPO tunable between 440 and 710 nm. The infrared and visible beams are then coherently mixed at the same point of the functionalized surface of the prism, as illustrated in Fig. 1. The two input beams are $\mathcal{P}$-polarized and the $\mathcal{P}$-component of the SFG output beam is collected by photomultipliers after spatial and spectral filtering through a monochromator. Besides, in order to compensate for the intensity fluctuations of the laser source, the SFG signal of a reference ZnS crystal is acquired in the same conditions and used to normalize the SFG intensity of the sample.

Data availability

The data that support the plots within this paper and other findings of this study are available from the corresponding author upon reasonable request.

Received: 8 June 2018 Accepted: 12 October 2018
Published online: 02 November 2018

References

1. Brus, L. E. Electron-electron and electron-hole interactions in small semiconductor crystallites: the size dependence of the lowest excited electronic states. *J. Chem. Phys.* **80**, 4403–4409 (1984).
2. Masumoto, Y. & Sonobe, K. Size-dependent energy levels of CdTe quantum dots. *Phys. Rev. B* **56**, 9734–9737 (1997).
3. Wang, X. et al. Photoluminescence upconversion in colloidal CdTe quantum dots. *Phys. Rev. B* **68**, 125318 (2003).
4. Wuister, S. F., Swart, I., van Driel, F., Hickey, S. G. & de Mello Donegá, C. Highly luminescent water-soluble CdTe quantum dots. *Nano Lett.* **3**, 503–507 (2003).
5. Sapra, S. & Sarma, D. D. Evolution of the electronic structure with size in II-VI semiconductor nanocrystals. *Phys. Rev. B* **69**, 125304 (2004).
6. Law, M. et al. Determining the internal quantum efficiency of PbSe nanocrystal solar cells with the aid of an optical model. *Nano Lett.* **8**, 3904–3910 (2008).
7. Vanmaekelbergh, D. & Liljeroth, P. Electron-conducting quantum dot solids: novel materials based on colloidal semiconductor nanocrystals. *Chem. Soc. Rev.* **34**, 299–312 (2005).
8. Cooney, R. R., Sewall, S. L., Sagar, D. M. & Kambhampati, P. Gain control in semiconductor quantum dots via state-resolved optical pumping. *Phys. Rev. Lett.* **102**, 127404 (2009).
9. Umar, A. A., Reshak, A. H., Oyama, M. & Plucinski, K. J. Fluorescent and nonlinear optical features of CdTe quantum dots. *J. Mater. Sci. Mater. Electron.* **23**, 546–550 (2012).
10. Humbert, C. et al. Linear and nonlinear optical properties of functionalized CdSe quantum dots prepared by plasma sputtering and wet chemistry. *J. Colloid Interface Sci.* **445**, 69–75 (2015).
11. Heuff, R. F., Swift, J. L. & Cramb, D. T. Fluorescence correlation spectroscopy using quantum dots: advances, challenges and opportunities. *Phys. Chem. Chem. Phys.* **9**, 1870–1880 (2007).
12. Costa-Fernandez, J. M., Pereiro, R. & Sanz-Medel, A. The use of luminescent quantum dots for optical sensing. *Trends Anal. Chem.* **25**, 207–218 (2006).

13. Tyrakowski, C. M. & Snee, P. T. A primer on synthesis, water-solubilization, and functionalization of quantum dots, their use as biological sensing agents, and present status. *Phys. Chem. Chem. Phys.* **16**, 837–855 (2014).
14. Wegner, K. D. & Hildebrandt, N. Quantum dots: bright and versatile in vitro and in vivo fluorescence imaging biosensors. *Chem. Soc. Rev.* **44**, 4792–4834 (2015).
15. Yong, K.-T. et al. Aqueous phase synthesis of CdTe quantum dots for biophotonics. *J. Biophotonics* **4**, 9–20 (2011).
16. Li, J. & Zhu, J.-J. Quantum dots for fluorescent biosensing and bio-imaging applications. *Analyst* **138**, 2506–2515 (2013).
17. Efros, A. L. & Rosen, M. Quantum size level structure of narrow-gap semiconductor nanocrystals: effect of band coupling. *Phys. Rev. B* **58**, 7120–7135 (1998).
18. Ajiki, H., Tsuji, T., Kawano, K. & Cho, K. Optical spectra and exciton-light coupled modes of a spherical semiconductor nanocrystal. *Phys. Rev. B* **66**, 245322 (2002).
19. Trani, F., Ninno, D. & Iadonisi, G. Tight-binding formulation of the dielectric response in semiconductor nanocrystals. *Phys. Rev. B* **76**, 085326 (2007).
20. Demchenko, D. O. & Wang, L.-W. Optical transitions and nature of Stokes shift in spherical CdS quantum dots. *Phys. Rev. B* **73**, 155326 (2006).
21. Caram, J. R. et al. PbS nanocrystal emission is governed by multiple emissive states. *Nano Lett.* **16**, 6070–6077 (2016).
22. Voznyy, O. et al. Origins of stokes shift in PbS nanocrystals. *Nano Lett.* **17**, 7191–7195 (2017).
23. Liu, Y., Kim, D., Morris, O. P., Zhitomirsky, D. & Grossman, J. C. Origins of the stokes shift in PbS quantum dots: impact of polydispersity, ligands, and defects. *ACS Nano* **12**, 2838–2845 (2018).
24. Kuno, M., Fromm, D. P., Hamann, H. F., Gallagher, A. & Nesbitt, D. J. 'On'/'off' fluorescence intermittency of single semiconductor quantum dots. *J. Chem. Phys.* **115**, 1028–1040 (2001).
25. Voznyy, O. & Sargent, E. H. Atomistic model of fluorescence intermittency of colloidal quantum dots. *Phys. Rev. Lett.* **112**, 157401 (2014).
26. Efros, A. L. et al. Band-edge exciton in quantum dots of semiconductors with a degenerate valence band: dark and bright exciton states. *Phys. Rev. B* **54**, 4843–4856 (1996).
27. Rodina, A. V. & Efros, A. L. Radiative recombination from dark excitons in nanocrystals: activation mechanisms and polarization properties. *Phys. Rev. B* **93**, 155427–155441 (2016).
28. Fomin, V. M. et al. Photoluminescence of spherical quantum dots. *Phys. Rev. B* **57**, 2415–2425 (1998).
29. Boehme, S. C. et al. Density of trap states and auger-mediated electron trapping in CdTe quantum-dot solids. *Nano Lett.* **15**, 3056–3066 (2015).
30. Zhang, H., Zhou, Z. & Yang, B. The influence of carboxyl groups on the photoluminescence of mercaptocarboxylic acid-stabilized CdTe nanoparticles. *J. Phys. Chem. B* **107**, 8–13 (2003).
31. Frederick, M. T. & Weiss, E. A. Relaxation of exciton confinement in CdSe quantum dots by modification with a conjugated dithiocarbamate ligand. *ACS Nano* **4**, 3195–3200 (2010).
32. Liang, Y., Thorne, J. E. & Parkinson, B. A. Controlling the electronic coupling between CdSe quantum dots and thiol capping ligands via pH and ligand selection. *Langmuir* **28**, 11072–11077 (2012).
33. Kilina, S., Velizhanin, K. A., Ivanov, S., Prezhdo, O. V. & Tretiak, S. Surface ligands increase photoexcitation relaxation rates in CdSe quantum dots. *ACS Nano* **6**, 6515–6524 (2012).
34. Frederick, M. T., Amin, V. A. & Weiss, E. A. Optical properties of strongly coupled quantum dot-ligand systems. *J. Phys. Chem. Lett.* **4**, 634–640 (2013).
35. Jin, S. et al. Enhanced rate of radiative decay in CdSe quantum dots upon adsorption of an exciton-delocalizing ligand. *Nano Lett.* **14**, 5323–5328 (2014).
36. Lifshitz, E. Evidence in support of exciton to ligand vibrational coupling in colloidal quantum dots. *J. Phys. Chem. Lett.* **6**, 4336–4347 (2015).
37. Xu, F. et al. Impact of different surface ligands on the optical properties of PbS quantum dot solids. *Materials* **8**, 1858–1870 (2015).
38. Azpiroz, J. M. & Angelis, F. D. Ligand induced spectral changes in CdSe quantum dots. *ACS Appl. Mater. Interfaces* **7**, 19736–19745 (2015).
39. Giansante, C. et al. 'Darker-than-black' PbS quantum dots: enhancing optical absorption of colloidal semiconductor nanocrystals via short conjugated ligands. *J. Am. Chem. Soc.* **137**, 1875–1886 (2015).
40. Debellis, D., Gigli, G., ten Brinck, S., Infante, I. & Giansante, C. Quantum-confined and enhanced optical absorption of colloidal PbS quantum dots at wavelengths with expected bulk behavior. *Nano Lett.* **17**, 1248–1254 (2017).
41. Kambhampati, P. Unraveling the structure and dynamics of excitons in semiconductor quantum dots. *Acc. Chem. Res.* **44**, 1–13 (2011).
42. Yazdani, N. et al. Tuning electron-phonon interactions in nanocrystals through surface termination. *Nano Lett.* **18**, 2233–2242 (2018).
43. Schnitzenbaumer, K. J. & Dukovic, G. Comparison of phonon damping behavior in quantum dots capped with organic and inorganic ligands. *Nano Lett.* **18**, 3667–3674 (2018).
44. Kambhampati, P. On the kinetics and thermodynamics of excitons at the surface of semiconductor nanocrystals: are there surface excitons? *Chem. Phys.* **446**, 92–107 (2015).
45. Arnolds, H. & Bonn, M. Ultrafast surface vibrational dynamics. *Surf. Sci. Rep.* **65**, 45–66 (2010).
46. Zhang, Z., Piatkowski, L., Bakker, H. J. & Bonn, M. Ultrafast vibrational energy transfer at the water/air interface revealed by two-dimensional surface vibrational spectroscopy. *Nat. Chem.* **3**, 888–893 (2011).
47. Dalstein, L. et al. Revealing the interplay between adsorbed molecular layers and gold nanoparticles by linear and nonlinear optical properties. *J. Phys. Chem. C.* **119**, 17146–17155 (2015).
48. Caudano, Y. et al. Electron-phonon couplings at C_{60} interfaces: a case study by two-color, infrared-visible sum-frequency generation spectroscopy. *J. Electron Spectrosc. Relat. Phenom.* **129**, 139–147 (2003).
49. Tourillon, G. et al. Total internal reflection sum-frequency generation spectroscopy and dense gold nanoparticles monolayer: a route for probing adsorbed molecules. *Nanotechnology* **18**, 415301–415307 (2007).
50. Blanton, S. A., Leheny, R. L., Hines, M. A. & Guyot-Sionnest, P. Dielectric dispersion measurements of CdSe nanocrystal colloids: observation of a permanent dipole moment. *Phys. Rev. Lett.* **79**, 865–868 (1997).
51. Shim, M. & Guyot-Sionnest, P. Permanent dipole moment and charges in colloidal semiconductor quantum dots. *J. Chem. Phys.* **111**, 6955–6964 (1999).
52. Haug, H. & Koch, S. *Quantum Theory of the Optical and Electronic Properties of Semiconductors*, fifth edn. (World Scientific, Singapore 2009).
53. Zhuang, X., Miranda, P. B., Kim, D. & Shen, Y. R. Mapping molecular orientation and conformation interfaces by surface nonlinear optics. *Phys. Rev. B* **59**, 12632 (1999).
54. Medintz, I. L., Uyeda, H. T., Goldman, E. R. & Mattoussi, H. Quantum dot bioconjugates for imaging, labelling and sensing. *Nat. Mat.* **4**, 435–446 (2005).
55. Sperling, R. A. & Parak, W. J. Surface modification, functionalization and bioconjugation of colloidal inorganic nanoparticles. *Philos. Trans. R. Soc. A* **368**, 1333–1383 (2010).
56. Moreels, I., Fritzinger, B., Martins, J. C. & Hens, Z. Surface chemistry of colloidal pbse nanocrystals. *J. Am. Chem. Soc.* **130**, 15081–15086 (2008).
57. Grisorio, R., Debellis, D., Suranna, G. P., Gigli, G. & Giansante, C. The dynamic organic/inorganic interface of colloidal pbs quantum dots. *Angew. Chem. Int. Ed.* **55**, 6628–6633 (2016).
58. Anderson, N. C., Hendricks, M. P., Choi, J. J. & Owen, J. S. Ligand exchange and the stoichiometry of metal chalcogenide nanocrystals: spectroscopic observation of facile metal-carboxylate displacement and binding. *J. Am. Chem. Soc.* **135**, 18536–18548 (2013).
59. Noblet, T., Dreesen, L., Hottechamps, J. & Humbert, C. A global method for handling fluorescence spectra at high concentration derived from the competition between emission and absorption of colloidal CdTe quantum dots. *Phys. Chem. Chem. Phys.* **19**, 26559–26565 (2017).
60. Kett, P. J. N. et al. Structural changes in a polyelectrolyte multilayer assembly investigated by reflection absorption infrared spectroscopy and sum frequency generation spectroscopy. *J. Phys. Chem. B* **113**, 1559–1568 (2009).
61. Zhang, Y. & Clapp, A. Overview of stabilizing ligands for biocompatible quantum dot nanocrystals. *Sensors* **11**, 11036–11055 (2011).
62. Krause, M. M. & Kambhampati, P. Linking surface chemistry to optical properties of semiconductor nanocrystals. *Phys. Chem. Chem. Phys.* **17**, 18882–18894 (2015).
63. Hung, K.-K., Stege, U. & Hore, D. K. IR absorption, Raman scattering, and IR-Vis sum-frequency generation spectroscopy as quantitative probes of surface structure. *Appl. Spec. Rev.* **50**, 351–376 (2015).
64. Jethi, L., Mack, T. G. & Kambhampati, P. Extending semiconductor nanocrystals from the quantum dot regime to the molecular cluster regime. *J. Phys. Chem. C* **121**, 26102–26107 (2017).
65. Kovalenko, M. V., Scheele, M. & Talapin, D. V. Colloidal nanocrystals with molecular metal chalcogenide surface ligands. *Science* **324**, 1417–1420 (2009).
66. Wolcott, A. et al. Anomalously large polarization effect responsible for excitonic red shifts in PbSe quantum dot solids. *J. Phys. Chem. Lett.* **2**, 795–800 (2011).
67. Swenson, N. K., Ratner, M. A. & Weiss, E. A. Computational study of the resonance enhancement of Raman signals of ligands adsorbed to CdSe clusters through photoexcitation of the cluster. *J. Phys. Chem. C* **120**, 20954–20960 (2016).
68. Sengupta, S., Bromley, L. & Velarde, L. Aggregated states of chalcogenorhodamine dyes on nanocrystalline titania revealed by doubly resonant sum frequency spectroscopy. *J. Phys. Chem. C* **121**, 3424–3436 (2017).
69. Lombardi, J. R. & Birke, R. L. Theory of surface-enhanced raman scattering in semiconductors. *J. Phys. Chem. C* **118**, 11120–11130 (2014).
70. Barbillon, G., Noblet, T., Busson, B., Tadjeddine, A. & Humbert, C. Localised detection of thiophenol with gold nanotriangles highly structured as honeycombs by nonlinear Sum Frequency Generation spectroscopy. *J. Mater. Sci.* **53**, 4554–4562 (2018).

Acknowledgements

Research leading to these results has received funding from the International Scientific Cooperation Program of the CNRS (Centre National de la Recherche Scientifique) under Grant agreement number PICS07339. The authors acknowledge Assistant Engineer B. Rieul (University of Paris-Sud, Université Paris-Saclay, Laboratoire de Chimie Physique, CNRS, 91405 Orsay, France) for his technical assistance on the pilot control development of the SFG spectroscopy setup, and Research Engineer P. Beaunier (Sorbonne Université, CNRS, Laboratoire de Réactivité de Surface, 75005 Paris, France) for her precious help in the realization and interpretation of EDX measurements.

Author contributions

The manuscript was achieved through contributions of all authors. T.N., L.D. and C.H. designed the sample configuration for UV-vis and 2C-SFG spectroscopy, and performed the 2C-SFG measurements. T.N. performed the UV-visible and EDX measurements, analyzed all the data and wrote the manuscript. T.N. also derived the analytical calculation of the second-order susceptibility to account for 2C-SFG measurements. C.M. and S.B. designed and performed the experiments for surface characterization and assembled the XPS data. T.N., L.D., S.B., C.M., B.B., A.T. and C.H. participated to the analysis and interpretation of the data and contributed to discussions and corrections during the writing process. L.D. and C.H. initiated and supervised the project.

Additional information

Supplementary information accompanies this paper at https://doi.org/10.1038/s42004-018-0079-y.

Competing interests: The authors declare no competing interests.

Reprints and permission information is available online at http://npg.nature.com/reprintsandpermissions/

Publisher's note: Springer Nature remains neutral with regard to jurisdictional claims in published maps and institutional affiliations.

Open Access This article is licensed under a Creative Commons Attribution 4.0 International License, which permits use, sharing, adaptation, distribution and reproduction in any medium or format, as long as you give appropriate credit to the original author(s) and the source, provide a link to the Creative Commons license, and indicate if changes were made. The images or other third party material in this article are included in the article's Creative Commons license, unless indicated otherwise in a credit line to the material. If material is not included in the article's Creative Commons license and your intended use is not permitted by statutory regulation or exceeds the permitted use, you will need to obtain permission directly from the copyright holder. To view a copy of this license, visit http://creativecommons.org/licenses/by/4.0/.

© The Author(s) 2018